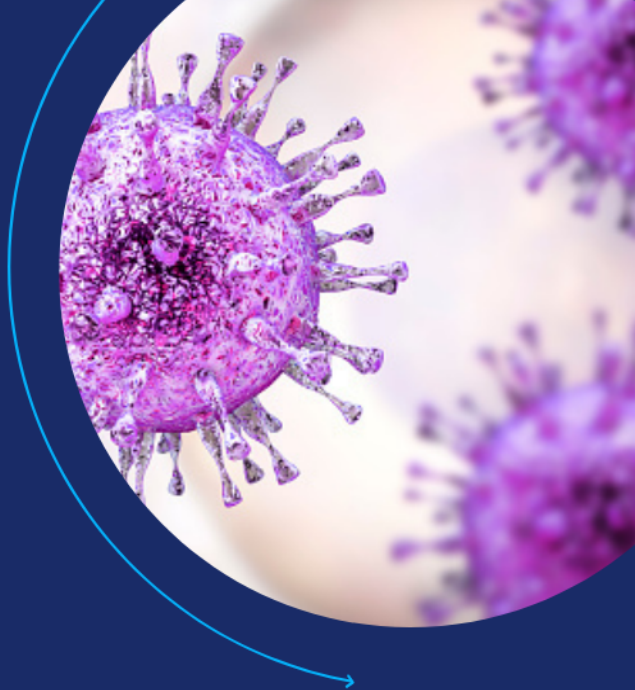# Putting SARS-CoV-2 where it belongs: Identification of potential therapeutic targets with single cell analysis

Respiratory failure is the most common adverse outcome for COVID-19 patients, but scientists and doctors are still searching for answers to the clinical complications of SARS-CoV-2 infection arising in other organs in the body, including the metabolic, cardiac, neurological, and gastrointestinal systems. Moreover, studies of SARS-CoV-2 infection mechanisms have relied on ACE2-overexpressing cells, masking the potential role of other factors in viral entry. Thus, there is an urgent need to create novel models using human disease-relevant cells to study SARS-CoV-2 biology and to facilitate drug screening.

## Free Webinar
November 11, 2020
9 am PST | 12 pm EST | 6 pm CET

Sponsored by:

10x GENOMICS

CURRENT PROTOCOLS
A Wiley Brand

Provided by:

WILEY

Basic

European Journal of **Immunology**

**Tissue immunology and leukocyte trafficking**

## Research Article

# Fetal-derived macrophages persist and sequentially maturate in ovaries after birth in mice

*Heli Jokela[1,3]* (iD)*, Emmi Lokka*[1,2,3], Miikka Kiviranta*[1], Sofia Tyystjärvi[1],
Heidi Gerke[1,3], Kati Elima[1,2], Marko Salmi**[1,2] and Pia Rantakari**[1,3]

[1] Institute of Biomedicine, University of Turku, Turku, Finland
[2] MediCity Research Laboratory, University of Turku, Turku, Finland
[3] Turku Bioscience Centre, University of Turku and Åbo Akademi University, Turku, Finland

Macrophages, which are highly diverse in different tissues, play a complex and vital role in tissue development, homeostasis, and inflammation. The origin and heterogeneity of tissue-resident monocytes and macrophages in ovaries remains unknown. Here we identify three tissue-resident monocyte populations and five macrophage populations in the adult ovaries using high-dimensional single cell mass cytometry. Ontogenic analyses using cell fate mapping models and cell depletion experiments revealed the infiltration of ovaries by both yolk sac and fetal liver-derived macrophages already during the embryonic development. Moreover, we found that both embryonic and bone marrow-derived macrophages contribute to the distinct ovarian macrophage subpopulations in the adults. These assays also showed that fetal-derived MHC II-negative macrophages differentiate postnatally in the maturing ovary to MHC II-positive cells. Our analyses further unraveled that the developmentally distinct macrophage types share overlapping distribution and scavenging function in the ovaries under homeostatic conditions. In conclusion, we report here the first comprehensive analyses of ovarian monocytes and macrophages. In addition, we show that the mechanisms controlling monocyte immigration, the phenotype of different pools of interstitial macrophages, and the interconversion capacity of fetal-derived macrophages in ovaries are remarkably different from those seen in other tissue niches.

**Keywords:** Developmental origin · Macrophages · Mass cytometry · Monocytes · Ovaries

📄 Additional supporting information may be found online in the Supporting Information section at the end of the article.

## Introduction

Macrophages are the most abundant immune cell population within the ovaries [1, 2], in which different types of ovum-containing and empty follicles are embedded in a highly vascularized interstitial. Ovarian macrophages (oMφ) are localized to the thecal, luteal, and atretic follicles and to the interstitial tissue [1–6]. oMφ are proposed to regulate vascularization, steroid production, epithelial cell proliferation, and differentiation, as well as tissue remodeling during normal follicle growth, ovulation, and luteinization [1, 2, 7–15]. Notably, female *Op/op* mice, which have an inactivating mutation in the major macrophage

growth factor gene *Csf1* [16], are subfertile. They manifest with a severe reduction of macrophages in most tissues including ovaries, decreased number of growing follicles [17], and a low pregnancy rate [18]. Systemic ablation of macrophages in CD11b-diphtheria toxin receptor transgenic mouse model leads to decreased vascular integrity, follicular atresia, and necrosis in ovaries [19, 20]. There is also emerging evidence that macrophages are involved in ovarian dysfunctions, particularly in polycystic ovary syndrome and premature ovarian failure, but also in endometriosis [14, 21, 22].

Historically, all macrophages have been thought to originate from bone marrow-derived circulating monocytes [23, 24]. However, more recent studies have revealed a complex diversity of tissue-resident macrophages, which include embryonic yolk sac and fetal liver-derived cells that are maintained locally and independently of blood monocytes [25–30].

Most studies with oMφ [1, 2, 7–15] date back to the time when the developmental, phenotypical, and functional heterogeneity of tissue-resident macrophages was not yet understood. Therefore, we took advantage of the current technological advancements to comprehensively examine the oMφ. These analyses revealed for the first time the coexistence of developmentally distinct macrophage subpopulations in the adult ovaries, and the interconversion capacity of the different interstitial macrophage types.

## Results

### Single-cell analysis identifies multiple tissue-resident monocyte and macrophage populations in postnatal ovaries

To explore the diversity of immune cell populations (live CD45$^+$ cells) in the ovaries, we employed single-cell mass cytometry (CyTOF) with comprehensive staining panel (Supporting information Fig. S1A,B). When high-dimensional single-cell data from 5-week-old (juvenile) and 12-week-old (adult) mouse ovaries were visualized on a two-dimensional map using tSNE (*t*-distributed stochastic neighbor embedding algorithm) [31], we found that majority of postnatal ovarian CD45$^+$ cells were CD11b$^+$ myeloid cells both in 5-week-old (58.8 ± 9.47%, n = three pools/three mice in each pool) and 12-week-old (52.6 ± 8.09%, n = three pools/three mice in each pool) mice (Supporting information Fig. S1B,C). Further downstream analysis revealed previously unknown subsets of CD45$^+$CD11b$^+$ myeloid cells in the postnatal ovaries (Supporting information Fig. S1D). We identified a dominant myeloid cluster coexpressing core macrophage markers F4/80 and CD64 both in 5- and 12-week-old mice (Supporting information Fig. S1D), and putatively assigned these F4/80$^+$CD64$^+$ cells as monocytes/macrophages cells (hereafter called MO/MAC; for the gating strategy see Fig. 1A).

Interestingly, of the core macrophage markers, CX3CR1 was expressed at varying levels on all MO/MAC cells but MerTK was found only on a few subpopulations (Fig. 1B). Several F4/80$^+$CD64$^+$ cell populations expressed high levels of Ly6C

(indicative of monocytes), and these populations had remarkably different levels of MHC II expression. Similarly, the Ly6C negative MO/MAC cell populations were clearly divided into several subpopulations based on the expression levels of CD11b, F4/80, MHC II, Siglec1, and CD206 (Fig. 1B). Unsupervised FlowSOM analyses [32] verified that three putative monocyte populations (assigned MONO 1–3) and three main putative macrophage populations (assigned MAC 1–3) were identifiable among ovarian MO/MAC cells both in 5- and 12-week-old mice (Fig. 1C).

Among the ovarian monocyte populations, MONO 1 expressed the lowest, MONO 2 intermediate, and MONO 3 the highest level of MHC II (Fig. 1B–D) both in 5- and 12-week-old mice. MONO 3 subpopulation was the most frequent monocyte subset both in 5- and 12-week-old mice, and its frequency significantly increased during aging (Fig. 1E). Since the expanding MONO 3 population expressed the highest level of MHC II, Siglec1, and MerTK and the lowest level of Ly6C among the monocytes, it may represent tissue-resident monocytes that have differentiated the furthest toward macrophages. Notably, the majority of Ly6C$^+$ monocytes fell into the MO/MAC-population in both 5- and 12-week-old mice (Supporting information Fig. S2A,B). The remaining Ly6C$^+$ monocytes falling outside the MO/MACs are in population called non-MO/MAC. Non-MO/MAC population included Ly6G$^+$ cell population (tentative granulocytes; 5 week 7.9 ± 0.68% and 12 week 6.3 ± 0.31%, n = three pools/three mice in each pool) and CD11c$^+$MHC II$^+$ cells, likely presenting dendritic cells (Supporting information Fig. S2C). In addition, further analyses of non-MO/MAC CD11c$^+$ cells revealed the presence of classical (F4/80$^-$CD64$^-$Ly6G$^-$CD4$^-$B220$^-$CD11c$^{high}$MHC II$^{high}$) and plasmacytoid (F4/80$^-$CD64$^-$Ly6G$^-$CD4$^-$B220$^+$CD11c$^+$CD11b$^-$) dendritic cell population in the ovaries of both 5- and 12-week-old mice (Supporting information Fig. S2A and D).

Unsupervised clustering revealed that among the ovarian macrophage populations, MAC 1 cells had very low levels of MHC II expression, while MAC 2 cells displayed intermediate MHC II expression, and MAC 3 cells high levels of MHC II expression (Fig. 1B–D). Notably, MAC 1 cells showed the highest F4/80 expression and the lowest CD11b expression, and MAC 3 cells the lowest F4/80 and the highest CD11b expression among the three MAC subpopulations (Fig. 1B,C). MAC 1 cells were practically devoid of MerTK, but expressed Siglec1. In fact, MAC 1 cells were further divided into three subclusters (MAC 1A-C) by the unsupervised FlowSOM analyses (Fig. 1C). Among MAC 1 cells, MAC 1A cells displayed the lowest and MAC 1C cells the highest levels of MHC II and CD206 in 5-week-old mice (Fig. 1D). The same expression profile was seen in ovarian MAC 1 subpopulations in 12-week-old mice, although the frequency of all MAC 1 cells among CD64$^+$F4/80$^+$ cells was significantly lower in 12-week-old mice (5.0 ± 1.18%, n = three pools/three mice in each pool) when compared to 5-week-old mice (Fig. 1E; 22.1 ± 3.78%, n = three pools/three mice in each pool). MAC 2 and MAC 3 populations, on the other hand, showed higher CD11c and MerTK levels when compared to MAC 1 cells (Fig. 1B–D). In contrast to MAC 1, the frequencies of MAC 2 and MAC 3 populations remained stable during the ovarian maturation, and both subpopulations
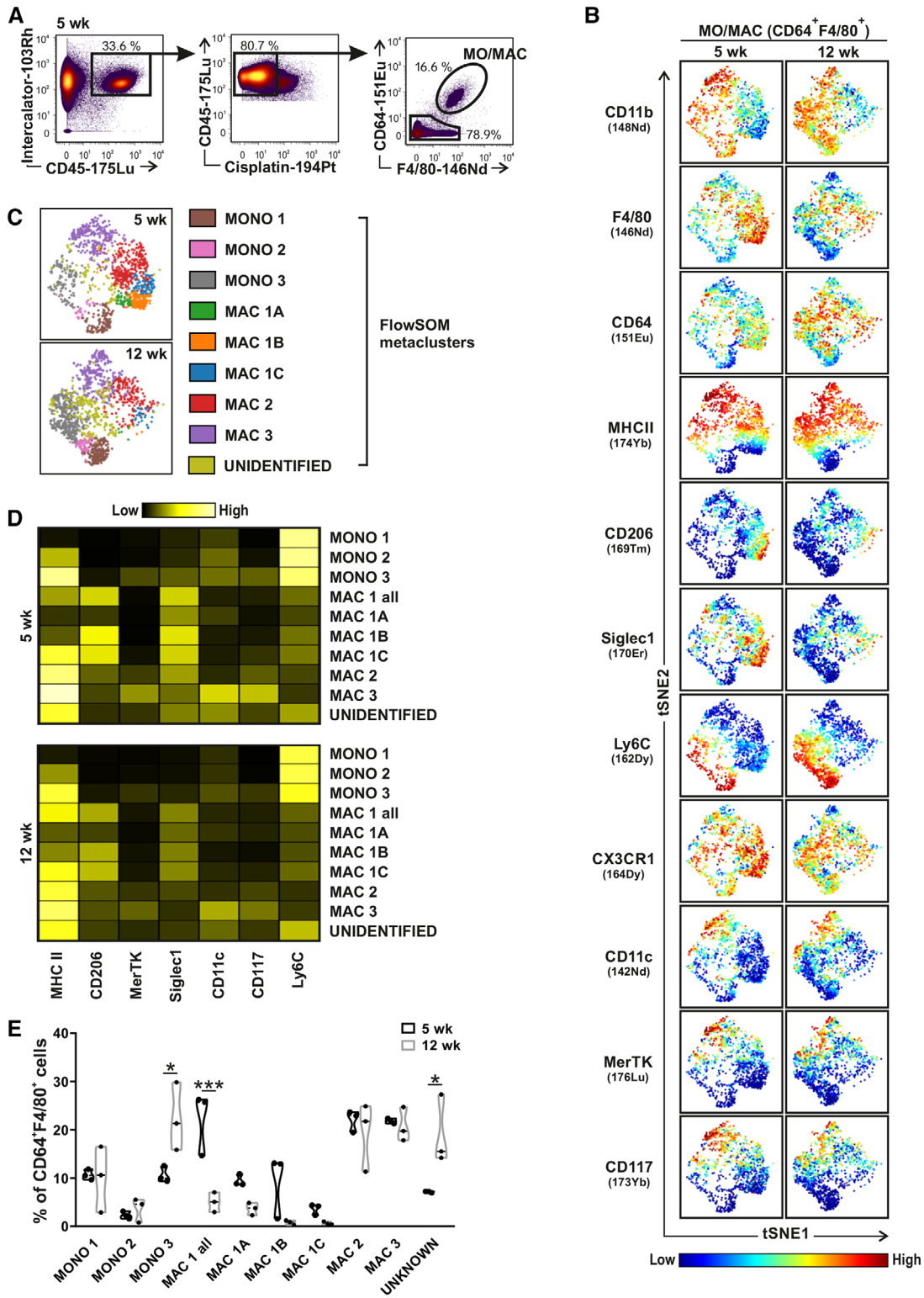
**Figure 1.** Multiple resident monocyte and macrophage populations in the ovaries. (A) Gating strategy for MO/MAC (CD64$^+$F4/80$^+$) cell mass cytometry analyses. (B) Mass cytometry analyses of resident CD64$^+$F4/80$^+$ myeloid cells in 5- and 12-week-old WT mice. The expression of the given markers is color-coded (blue means low and red high expression) on the $t$-distributed stochastic linear embedding ($t$-SNE) map. (C) Unsupervised FlowSOM analyses of resident CD64$^+$F4/80$^+$ myeloid cell clusters in the ovaries. The distinct metaclusters are shown in different colors. (D) Heat map analyses (from C) showing the mean expression of indicated markers (black means low and bright yellow high expression). (E) Frequencies of the resident ovarian CD64$^+$F4/80$^+$ myeloid cell types (from B). Violin plots represent mean $\pm$ SEM of each group ($^*p < 0.05$, $^{***}p < 0.001$ Kruskal–Wallis test followed with Dunn's post-hoc test). All mass cytometry data are from three independent experiments, in which ovaries from three mice were pooled together.

represented about 21% of MO/MAC cells both in 5- and 12-week-old mice (Fig. 1E). Collectively, these mass cytometric analyses show the dynamic coexistence of multiple tissue-resident monocyte and macrophage types in juvenile and adult ovaries, and show the value of MHC II expression in defining these distinct subpopulations.

## Kinetic changes in macrophage subpopulations in postnatal ovaries

We further characterized the kinetics of the postnatal ovarian macrophages ($CD45^+CD64^+F4/80^+Ly6C^-$ cells) in young mice by conventional flow cytometry, which is compatible with the low cell numbers recovered from the small organs (Supporting information Fig. S3A). Biaxial gating of the mass cytometric data from selected time points confirmed the validity of the gating strategy used in the fluorimetric analyses (Supporting information Fig. S3B). The flow cytometric analyses revealed that MHC $II^-$ MAC 1 cells were the only oMφ subpopulation already present in newborn (NB) ovaries (Fig. 2A,B). After 1 week of postnatal life, MAC 1 remained the only detectable macrophage type, and it still represented more than 70% of all ovarian macrophages in 2-week-old mice. Thereafter, the frequency of MAC 1 cells decreased to the 30-40% levels seen in 5-week-old and older animals. While the frequency of MAC 1 cells decreased in the maturing ovaries, the absolute numbers of MAC 1 cells slightly increased during the development in line with the increase in the size of the organ (NB 85 ± 25 cells/ovary, n = 5 mice; 5 week 111 ± 24 cells/ovary, n = 9 mice and 12 week 122 ± 30 cells/ovary, n = 7 mice, Supporting information Fig. S3C). The $CD206^+$ and $CD206^{neg/low}$ cells within the MAC 1 cells were equally abundant at birth, and their frequencies remained fairly stable during the postnatal development (Supporting information Fig. S3D). On the other hand, the two MHC $II^+$ populations, MAC 2 and MAC 3, emerged only at 2 weeks of age and thereafter markedly increased in the maturing ovaries (Fig. 2A,B and Supporting information S3C). Among the ovarian monocyte populations, only MHC $II^-Ly6C^+$ cells were identifiable in the ovaries of NB, 1- and 2-week-old mice, and at each time point they represented about 10% of all $CD45^+$ cells. Thus, at birth only MHC II negative monocytes and macrophages are present in the ovaries. While the absolute numbers of all three main macrophage populations then increase in the ovaries during aging, their frequencies display characteristic changes during the postnatal maturation of the virgin mouse.

## Ovarian macrophage subpopulations show overlapping subtissular localization and scavenging functions

We then studied the localization and function of the major macrophage populations in the ovaries using whole-mount and vibratome section stainings of optically cleared tissue. In NBs, $F4/80^+MHC$ $II^-$ cells distributed throughout the stromal compartment and around the follicles, and many cells were in close
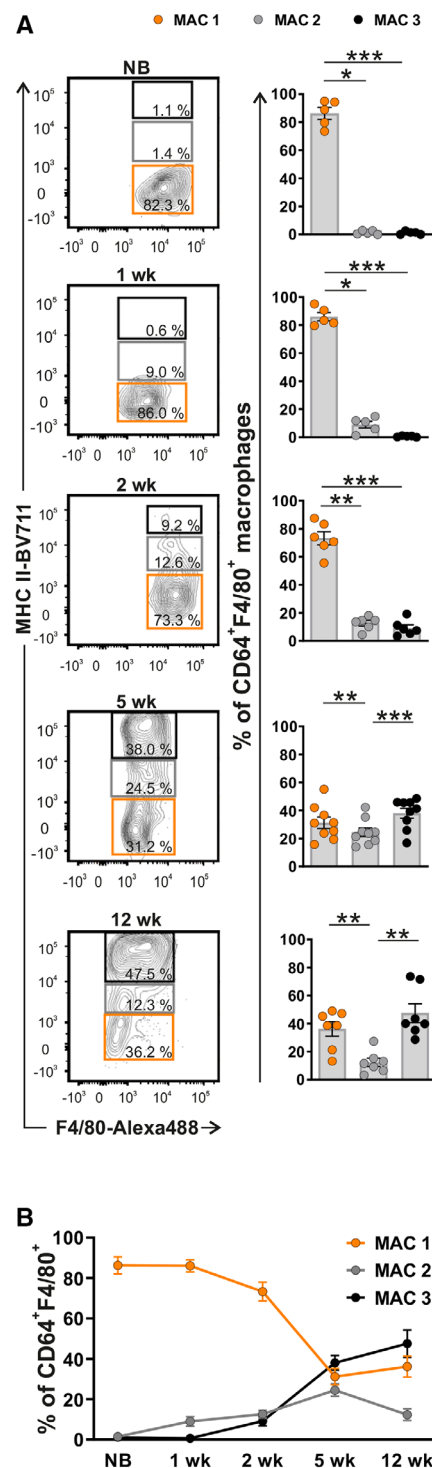


**Figure 2.** Developmental induction of MHC II on ovarian macrophages. (A) Flow cytometric analyses of tissue-resident ovarian macrophage populations in newborn (NB; n = 5), 1 week (n = 5), 2 weeks (n = 6), 5 weeks (n = 9), and 12 weeks (n = 7) old WT mice. Shown are representative flow cytometry plots and quantifications of MAC 1 (MHC $II^{neg/low}$; orange gates), MAC 2 (MHC $II^{int}$; grey gates), and MAC 3 (MHC $II^{high}$; black gates) macrophage populations among live $CD64^+F4/80^+$ myeloid cells. (B) The frequencies of ovarian macrophage populations (MAC 1–3) at the indicated postnatal time points. Bars represent the mean ± SEM of each group (*$p < 0.05$, **$p < 0.01$, ***$p < 0.001$ Kruskal–Wallis test followed with Dunn's post-hoc test). All data are from two independent experiments.
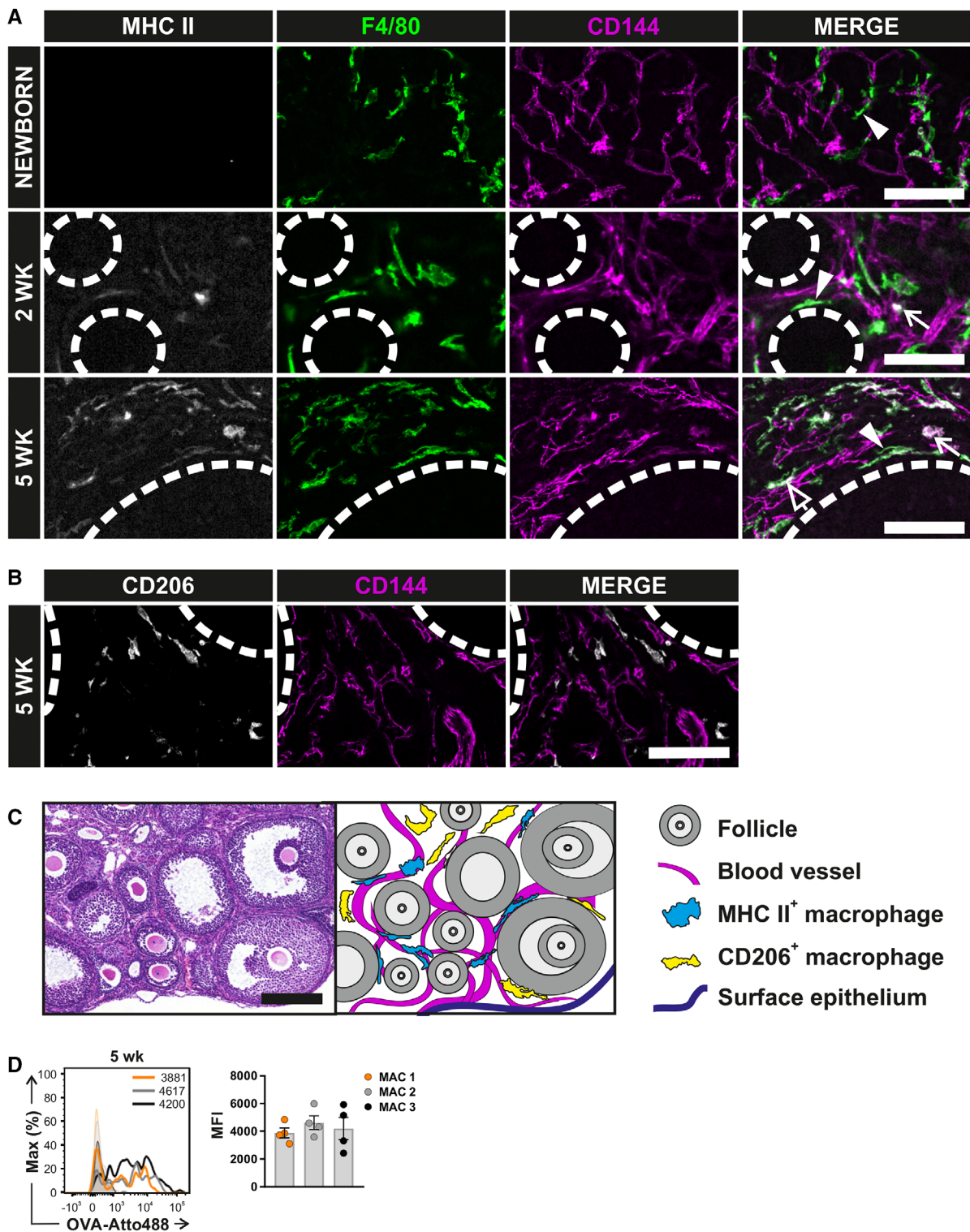
**Figure 3.** Intraorgan localization and scavenging functions of ovarian macrophage subpopulations. (A) Immunofluorescent detection of MHC II, F4/80 and CD144 in the whole-mount ovary samples of newborn, 2- and 5-week-old WT mice. Representative MHC II$^{high}$F4/80$^{neg}$ cells (arrow), MHC II$^{neg}$F4/80$^{high}$ cells (white arrow head), and MHC II$^{high}$F4/80$^{pos}$ cells (open arrow head). (B) Immunofluorescent detection of CD206 and CD144 in the ovaries of 5-week-old WT mice. Dashed lines represent the edge of the follicles. Images were acquired with 40× magnification. Scale bar 50 μm. (C) Ovarian histology of 5-week-old WT female together with schematic illustration of macrophage localization in the ovaries. Image was acquired with 20× magnification. Scale bar 200 μm. (D) Uptake of intravenously administered fluorescent ovalbumin immunocomplexes (OVA-SIC) by MAC 1, MAC 2, and MAC 3 macrophage subpopulations in the ovaries of 5-week-old WT mice and measured by flow cytometry. Shown are representative histograms (controls as filled) and quantification of the data (mean ± SEM, n = 4 mice). Data are from two independent experiments. Control mice received PBS injections. MFI, mean fluorescence intensity.

association with CD144$^+$ blood vessels (Fig. 3A,C, and Supporting information Fig. S4A). At 2 and 5 weeks of age, both elongated F4/80$^+$MHC II$^-$ and F4/80$^+$MHC II$^+$ cells, likely representing MONO 1/MAC 1 and pooled MONO 2/MAC 2+MONO 3/MAC 3 populations, were found around the follicles and in intimate contacts with the vasculature. No obvious differences in the intraorgan distribution of these two cell types were identifiable. Interestingly, most CD206$^+$ macrophages, identified as a perivascular macrophage type in several other tissues [33–35], had no apparent contacts to the vasculature in the ovaries (Fig. 3B,C and Supporting information Fig. S4B).

To analyze the possible functional differences of oMφ populations in vivo, we injected i.v. a premade OVA-anti-OVA antibody immunocomplex (SIC) to 5-week-old WT mice. In flow cytometric assays, MAC 1, MAC 2, and MAC 3 cells showed a comparable capacity to bind/uptake SIC from the blood (Fig. 3D). Interestingly, unlike reported in other tissues, CD206$^+$ MAC 1 macrophage population did not bind/uptake SIC any better than the CD206$^{low/neg}$ MAC 1 macrophage subpopulations (Supporting information Fig. S4C). Collectively, these data suggest that the different macrophage populations display comparable tissue distribution and largely overlapping scavenging function in the ovaries.

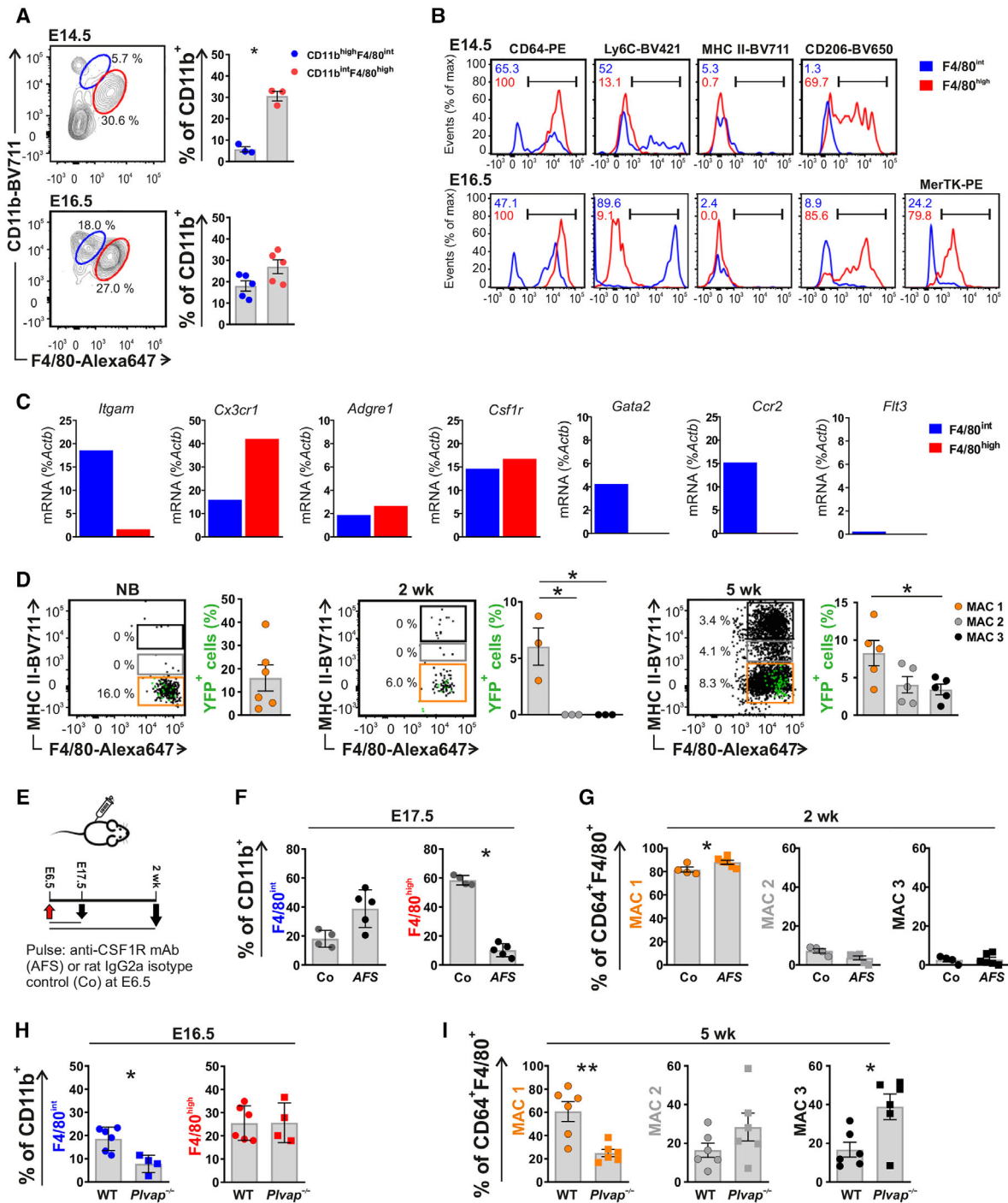## Embryonic macrophages persist in adult ovaries

Given the marked heterogeneity and kinetic changes in oMφ populations, we hypothesized that both embryonically and postnatally derived cells could contribute to the macrophage pool in the adult ovaries. During embryonic development, CD11b$^{int}$F4/80$^{high}$ and CD11b$^{high}$F4/80$^{int}$ phenotypes are thought to be indicative of yolk sac-derived and fetal liver-derived macrophages, respectively [27, 36–40]. Using flow cytometry, we found a dominant CD11b$^{int}$F4/80$^{high}$ macrophage population in the ovaries at embryonic day 14.5 (E14.5), when CD11b$^{high}$F4/80$^{int}$ oMφ were almost absent (Fig. 4A and Supporting information Fig. S5A). In contrast, 2 days later at E16.5 the frequency of CD11b$^{high}$F4/80$^{int}$ cells was significantly increased (5.7 ± 1.21% at E14.5 vs. 18.0 ± 2.42% at E16.5, n = 3-5) and became almost similar to that of CD11b$^{int}$F4/80$^{high}$ cells (Fig. 4A). Thus, our data would be compatible with a scenario in which the embryonic ovaries are first infiltrated by yolk sac-derived macrophages and later superseded by fetal liver-derived macrophages.

At E14.5 CD11b$^{int}$F4/80$^{high}$, cells were CD64$^+$CD206$^+$ and Ly6C$^-$, whereas the rare CD11b$^{high}$F4/80$^{int}$ cells were CD206$^-$ and mostly CD64$^-$, but contained a clear Ly6C$^+$ subpopulation (Fig. 4B). This phenotype would be consistent with the monocyte-independent and monocyte-dependent generation of yolk sac and fetal liver macrophages, respectively. At E16.5, CD11b$^{high}$F4/80$^{int}$ cells had become uniformly Ly6C$^+$, but remained CD206$^-$ and MerTK$^-$. CD11b$^{int}$F4/80$^{high}$ cells, in contrast, were brightly CD206$^+$ and MerTK$^+$. Notably, both fetal macrophage populations were completely MHC II negative (Fig. 4B). When E16.5 oMφ were sorted and subjected to mRNA expression analyses,

both CD11b$^{int}$F4/80$^{high}$ and CD11b$^{high}$F4/80$^{int}$ macrophage populations were found to express transcripts for the macrophage core genes Cx3cr1, Adgre1, Csf1r, and Itgam. In contrast, only CD11b$^{high}$F4/80$^{int}$ cells expressed Gata2 and Ccr2 (Fig. 4C). Both cell types lacked dendritic cell-specific Flt3 expression, confirming their macrophage identity. Collectively, these data are consistent with the scenario that CD11b$^{int}$F4/80$^{high}$ cells also in fetal ovaries represent yolk sac-derived macrophages, and CD11b$^{high}$F4/80$^{int}$ cells are fetal liver monocyte-derived macrophages, which gradually replace the yolk sac-derived cells.

To investigate the embryonic origin oMφ populations in more detail, we performed fate mapping experiments. In CX3CR1$^{CreERT2}$;R26R-EYFP reporter mouse model (Fig 4D and Supporting information Fig. S5B) tamoxifen-induced labelling at E13.5 allows identification of yolk sac-derived macrophages [27, 37, 41]. We observed yellow fluorescent protein positive (YFP$^+$) cells in the ovaries of NB, 2- and 5-week-old mice (Fig. 4D). The frequency of embryonic yolk sac-derived YFP$^+$ cells among all oMφ only slightly decreased after birth. The majority of YFP$^+$ cells fell into the MHC II$^-$ MAC 1 population at all time points studied. Markedly however, YFP$^+$ cells were also clearly identifiable in MHC II$^{int}$ MAC 2 and MHC II$^{high}$ MAC 3 populations in the ovaries of 5-week-old mice. We also used CSF1R$^{Mer-iCre-Mer}$; R26R-EYFP-reporter mice to label yolk sac-derived macrophages by tamoxifen administration to dams at pregnancy day 8.5 [36]. The inclusion of yolk sac-derived YFP$^+$ cells in all three macrophage subpopulations in 5-week-old mice was confirmed with this second genetic fate mapping model (Supporting information Fig. S5C). The phenotypic and fate mapping analysis, thus, strongly argue for an interconversion of ovarian macrophage types in postnatal mice.

To study how depletion of yolk sac-derived macrophages affects oMφ populations, we gave a single injection of anti-CSF1R antibody (clone AFS98; Bio X Cell) or rat IgG2a control antibody (clone 2A3; Bio X Cell) to the pregnant WT dams at E6.5 (Fig. 4E). Consistently with the previous literature [42, 43], the anti-CSFR1 antibody depleted all yolk sac-derived CD45$^+$F4/80$^+$ macrophages in the fetal brain (Supporting information Fig. S5D). We found that anti-CSFR1 antibody also caused a significant reduction in the frequency of CD11b$^{int}$F4/80$^{high}$ macrophages, and a concomitant increase in the frequency of CD11b$^{high}$F4/80$^{int}$ macrophages, in the ovaries of E17.5 embryos (Fig. 4F). However, the successful depletion of yolk sac-derived macrophages had no significant effect on the frequency of different oMφ subpopulations in 2-week-old mice (Fig. 4G). Analysis of Plvap$^{-/-}$ mice, which show selective reduction of fetal liver-derived macrophages but normal yolk sac-derived macrophages [44], showed a selective reduction of F4/80$^{int}$ oMφ population in E16.5 mice (Fig. 4H). In 5-week-old Plvap$^{-/-}$ mice, we also found a reduction of MAC 1 population, and an increase in the frequency of MAC 2 and MAC 3 cells (Fig. 4I). Thus, our data suggest that both yolk sac and fetal liver contribute to the establishment of macrophage populations in the ovaries during the embryonic period, and that they both remain completely MHC II negative at birth. Moreover, our results show that at least fetal yolk sac-derived macrophages persist

### Bone marrow monocyte-derived macrophages infiltrate ovaries

Since the bone marrow-derived macrophages heavily contribute to postnatal macrophage pools in most organs, we attempted to address their contribution to the oMφ populations. To that end, we used *Ccr2-* and *Nur77-*deficient mice, which have low numbers in circulating Ly6C^{high} and Ly6C^{low} monocytes, respectively [45, 46]. Unexpectedly, the MAC 1, MAC 2, or MAC 3 macrophages in steady state virgin ovaries were unaffected by Ccr2 deficiency at 2, 5, and 12 weeks of age (Fig. 5A and Supporting information Fig. S6A,B). Moreover, bone marrow-derived patrolling Ly6C^{low} monocytes apparently did not contribute to the generation of any oMφ pool either, since the three macrophage populations were

until puberty, and that they can further differentiate to MHC II[+] MAC 2 and MAC 3 cells during maturation.

indistinguishable in the ovaries of WT and Nur77$^{-/-}$ mice (Fig. 5A and Supporting information Fig. S6A).

To gain insight to the entry of macrophages into an empty niche, we depleted tissue-resident macrophages with clodronate and anti-CSF1 antibody treatment using a previously described dosing regimen (Fig. 5B) [47, 48]. The cyclic treatment was started at postnatal day 14 and completed at day 23. Two days after the completion of the third treatment cycle, more than 93% of MAC 1, MAC 2, and MAC 3 were depleted from the ovaries (Fig. 5C; acute). At the same time, the bone marrow and blood monocyte numbers were normalized, as shown previously by us and others [47, 48]. During a 10-day recovery period, no marked recovery of any macrophage subpopulation was discernible (Fig. 5C). After a 3 week recovery, in contrast, MAC 1 population was fully recovered in comparison to the control treated animals, and the numbers of MHC II$^{+}$ MAC 2 and MAC 3 cells were also partially restored (Fig. 5C). MONO 1–3 populations were also effectively depleted by the clodronate + anti-CSF1 treatment and their recovery kinetics resembled those of macrophages (Supporting information Fig. S6B). Thus, after a 10-day recovery only minimal numbers of tissue-resident monocytes were observed in the ovaries, while after 3 weeks MONO 1, 2, and 3 populations were detectable at numbers comparable to control-treated mice. These data suggest that when an empty niche is generated in the postnatal ovaries, bone marrow-derived monocytes, in a CCR2-independent manner, are capable of regenerating all three tissue-resident macrophage types. Moreover, the first macrophages recovering during the postnatal infiltration of pre-empted ovarian niche have MHC II$^{neg}$ MAC 1 phenotype, which resembles the MHC II$^{neg}$ phenotype of the first naturally occurring oMφ during the fetal development.

To analyze the apparently complex developmental pathways of oMφ generation further in untouched WT mice, we performed unsupervised clustering analysis for single cell data (CD64$^{+}$F4/80$^{+}$ MO/MAC) with K-nearest neighbor density-based clustering algorithm called X-shift [49]. To visualize the results, clusters were subjected to a force-directed graph layout (Fig. 5D). Ly6C and MHC II expression was used to manually assign the clus-ters to different MONO and MAC populations. The three separate macrophage populations (MAC 1, 2, and 3) became apparent also in these analyses of ovaries from 5-week-old females. In addition, separate Ly6C$^{high}$ and Ly6C$^{low}$ tissue-resident monocyte populations were distinguishable. The trajectory analyses suggested that Ly6C$^{high}$ monocytes gave rise both to Ly6C$^{low}$ monocytes and to MAC 1 (Fig. 5D,E). On the other hand, Ly6C$^{low}$ monocytes had trajectories to both MAC 3 and MAC 2 cells. Notably, the MAC 1 cluster also had connectivity to the MAC 2 cluster, and there were strong associations between MAC 2 and MAC 3 clusters. In 12-week-old mice, the trajectory analyses suggested that the majority of Ly6C$^{high}$ tissue-resident monocytes differentiated via Ly6C$^{int}$ and Ly6C$^{low}$ populations to the three MAC subtypes, which were compacted more closely with each other than in 5-week-old mice (Supporting information Fig. S6C,D). The trajectory analyses, thus, suggest that Ly6C$^{+}$ monocytes, via different intermediates, can give rise to all three MAC subpopulations, and that MAC populations are also likely interconvertible.

## Discussion

Here we identified three major macrophage subsets with divergent gene expression profiles and distinct kinetics of appearance in the maturing postnatal ovaries. Both yolk sac and fetal liver-derived macrophages populated the ovaries during embryonic development. At birth, they both contributed to the single MHC II negative macrophage population identifiable in the ovaries. Genetic fate mapping analyses directly verified the persistence of embryonic yolk sac-derived macrophages in the ovaries for at least 5 weeks after birth. Importantly, the reporter mice also showed that the embryonically derived MHC II$^{neg}$ MAC 1 cells can further differentiate to MHC II positive MAC 2 and MAC 3 cells after birth. Our trajectory analyses and depletion experiments suggested that bone marrow-derived monocytes also contribute to the ovarian macrophage pool postnatally. Collectively our data imply that the ovarian microenvironment rather than the developmental origin is decisive in shaping the macrophage phenotype, localization, and

**Figure 4.** Embryonic-derived macrophages give rise to all macrophage subtypes in adult ovaries. (A) Flow cytometric analyses of CD11b$^{high}$F4/80$^{int}$ (blue gates) and CD11b$^{int}$F4/80$^{high}$ (red gates) macrophage populations in the ovaries of WT embryos at embryonic day (E) 14.5 and E16.5. In the quantifications, each dot represents data from two individual mice pooled together in E14.5 mice (n = 3 from one experiment) and from individual mice at E16.5 (n = 5 from two independent experiments). (B) Representative histograms of CD64, Ly6C, MHC II, CD206, and MerTK expression (from A). (C) Quantitative RT-PCR analysis of the indicated transcripts in CD11b$^{high}$F4/80$^{int}$ (blue gates) and CD11b$^{int}$F4/80$^{high}$ (red gates) macrophage populations sorted from the ovaries of E16.5 WT embryos. Data are from one experiment and the sorted populations were pooled from three different litters and from 12 individuals. The gene expression values of *Itgam*, *Cx3cr1*, *Adgre1*, *Csf1r*, *Gata2*, *Ccr2*, and *Flt3* are shown in relation to *Actb* control gene. (D) Representative flow cytometry plots and kinetic quantifications of yolk sac-derived macrophages in the ovaries. The plots show the backgating of the YFP$^{+}$ cells (green) on the different ovarian macrophage populations in Cx3cr1-EYFP reporter mice induced at E13.5 with tamoxifen. The quantifications show the frequency of YFP$^{+}$ cells in each macrophage population and conversion of MHC II$^{neg}$ embryonic macrophages to MHC II$^{high}$ macrophage subtypes. MAC 1 (MHC II$^{neg/low}$; orange gates), MAC 2 (MHC II$^{int}$; grey gates), and MAC 3 (MHC II$^{high}$; black gates). Data are mean ± SEM from n = 6 (NB mice), n = 5 (2-week-old mice) and n = 4 (5-week-old mice), and derived from two to three individual experiments. (E-G) Analyses of ovarian macrophages in WT mice treated with anti-CSF1R (AFS98) or control antibody at E6.5. Shown are (E) experimental design and (F) flow cytometry quantifications of CD11b$^{high}$F4/80$^{int}$ (blue gates) and CD11b$^{int}$F4/80$^{high}$ (red gates) macrophage population at the age of E17.5, and (G) MAC 1 (orange), MAC 2 (grey) and MAC 3 (black) populations at 2 weeks of age (n = 4-6 mice). Data are from two individual experiments. (H) Flow cytometric analyses of CD11b$^{high}$F4/80$^{int}$ (blue gate) and CD11b$^{int}$F4/80$^{high}$ (red gate) macrophage populations in the ovaries of E16.5 *Plvap*$^{-/-}$ embryos (n = 4-6). Data are from three individual experiments. (I) Flow cytometric analyses of MAC 1 (orange gates), MAC 2 (grey gates), and MAC 3 (black gates) macrophage populations in the ovaries of 5-week-old *Plvap*$^{-/-}$ mice (n = 6). Data are from five individual experiments. Bars represent the mean ± SEM of each group (*$p < 0.05$, Mann–Whitney test).
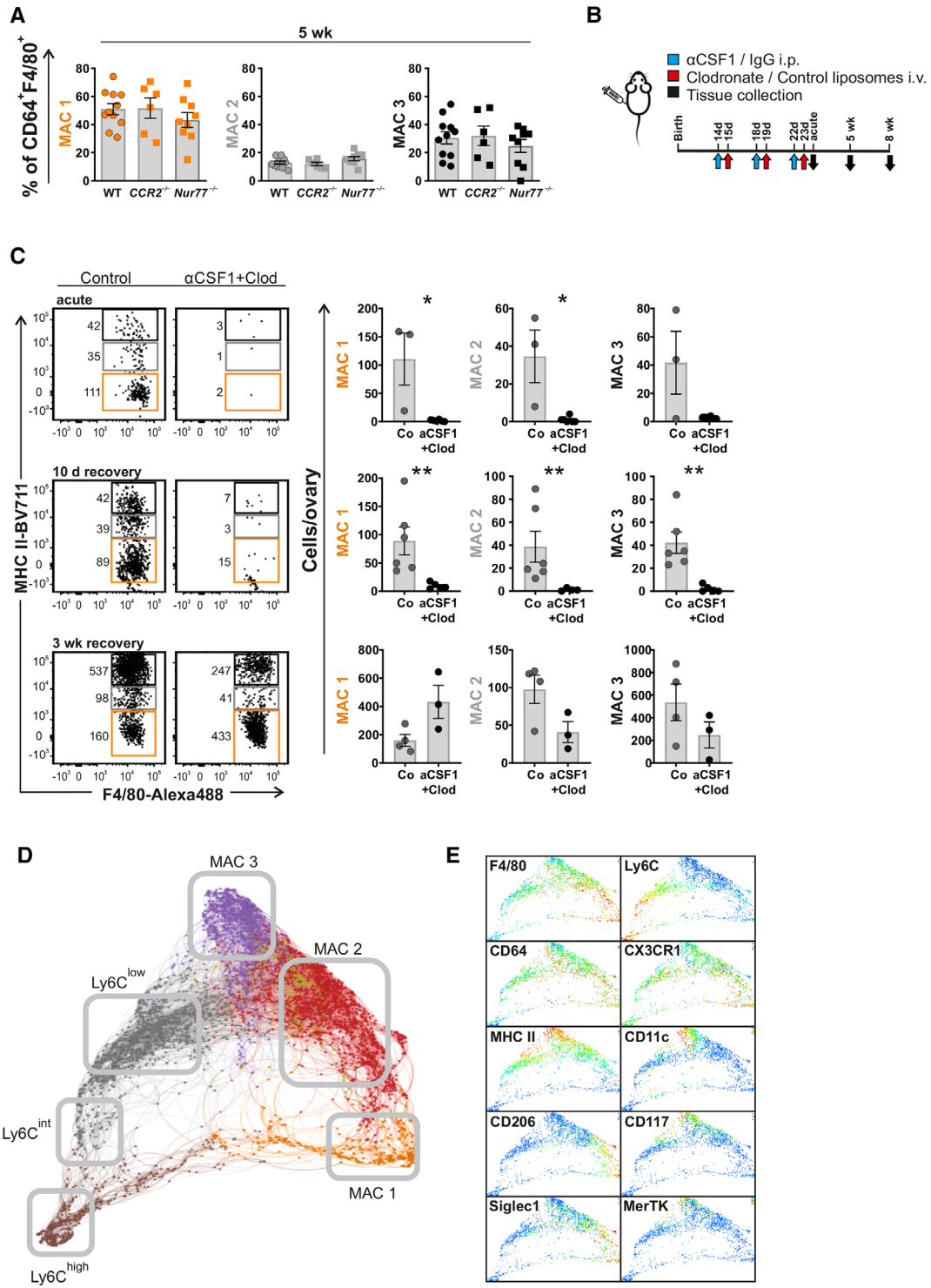
function. Moreover, our findings reveal several unique characteristics of tissue-resident macrophages in the ovaries when compared to those in other organs.

We propose that during organogenesis, the ovaries are colonized successively by yolk sac, fetal liver, and postnatal bone marrow-derived macrophages. Our phenotypic, fate mapping and anti-CSFR1 depletion studies showed that the first emerging macrophages in the fetal ovaries originate from the yolk sac. These cells develop without monocytic intermediates and seed fetal tissues starting from E8.5 after the development of functional vasculature [36]. After the emergence of hematopoietic stem cells (HSC) at E10.5, fetal liver starts to produce monocytes, which then exit to blood and seed to different tissues starting from E12.5 [42]. The arrival of these monocytes to the fetal ovaries

was supported by several findings. First, the frequency of Ly6C$^{high}$ cells substantially increased in ovaries from E14.5 to E16.5. Second, CD11b$^{high}$F4/80$^{int}$ macrophage population, phenotypically indicative of fetal liver-derived macrophages, was absent in E14.5 ovaries but frequently present in E16.5. Third, in *Plvap*$^{-/-}$ mice, which have normal production of yolk sac macrophages but a selective defect in the exit of fetal liver monocytes into blood [44], CD11b$^{high}$F4/80$^{low}$ population was diminished in ovaries. Since no genetic fate mapping tools are available, to our knowledge, for selective labelling of fetal liver-derived macrophages, direct demonstration of the migration and maintenance of this macrophage type in the ovaries remains to be done. Moreover, it is also possible that rare HSCs found in nonhematopoietic tissues [50–52] could locally give rise to monocytes in the ovaries, especially since the HSC-forming vasculature and the ovary-forming mesenchyme coexist in the aorta-gonad-mesonephros region [53]. In any case, our data suggest that monocyte-independent infiltration of the first ovarian macrophages is already during the later steps of embryogenesis followed by a second, monocyte-dependent phase of macrophage seeding to the ovaries.

Several lines of evidence suggest that bone marrow-derived monocytes contribute to the ovarian macrophage pool after birth. First, we found high frequency of Ly6C$^{high}$MHC II$^{neg}$ monocytes (MONO 1) in ovarian tissue still in 12-week-old mice, suggesting the presence of recent blood emigrants. Moreover, our trajectory analyses indicate that in juvenile 5-week-old mice, the tissue-resident Ly6C$^{hi}$ monocytes differentiate directly to MAC 1, or via Ly6c$^{low}$ intermediates to MAC 2 and 3. The trajectory analyses suggested that in 12-week-old mice, the Ly6C$^{high}$ tissue-resident monocyte population mainly gave rise to all three MAC subtypes via Ly6C$^{low}$ intermediates. Finally, when adult ovaries were experimentally emptied from monocytes and macrophages, all three macrophage populations eventually reappeared. However, we cannot fully exclude the possibility that the few depletion-resistant cells, possibly including fetal-derived cells, would regenerate the oMφ pools by vigorous local proliferation. Nevertheless, we can conclude that monocytes and macrophages from distinct developmental origins contribute to the heterogeneous macrophage pools seen in postnatal ovaries under physiological conditions.

Our observations strongly argue for the dominant role of tissue environment rather than ontogenic origin in shaping the ovarian macrophage pool. Very recently elegant analyses in lungs and multiple other tissues, including skin, fat, and heart, revealed the existence of two distinct interstitial macrophage populations [54]. Lyve-1$^{high}$MHC II$^{low}$ cells were found to represent perivascular macrophages, whereas Lyve-1$^{low}$MHC II$^{high}$ macrophages resided adjacent to nerves. In these analyses, Lyve-1$^{high}$ cells were CD206$^+$ and Lyve-1$^{low}$ cells were CD206$^-$. We and others have already earlier seen the preferential perivascular localization of Lyve1$^{high}$ or CD206$^+$ macrophages in mammary gland, lung, heart, fat, and skin [33–35, 48, 55]. The two populations now characterized by Ginhoux group were reported to originate from two separate lineages of monocytes [54]. Interestingly, we did not detect any apparent differences in the intraorgan localization of the three different oMφ subpopulations in ovaries. More specifically, we frequently observed MHC II$^{high}$ cells at the perivascular localization and CD206$^+$ cells at the nonperivascular locations in the ovaries. In ovaries, all three main macrophage populations also had comparable capacity to bind immunocomplexes from circulation. While the MHC II$^{high}$ macrophage populations in lung and ovaries share certain parameters (both were CD206$^{low/neg}$), they differed in others (e.g., lung cells were CX3CR1$^{high}$ while ovarian MAC 3 were mainly CX3CR1$^{low}$). Moreover, both lung interstitial macrophage populations were independently replaced by CCR2-dependent migration of Ly6C$^{high}$ monocytes rather than by interconversion of the two macrophage populations. In contrast, the emigration of fetal liver and bone marrow-derived monocytes to ovaries was completely CCR2-independent. Furthermore, our genetic fate mapping experiments with two different reporter systems unambiguously showed that at least yolk sac-derived oMφ MAC 1 cells differentiate to MAC 2 and MAC 3 cells in the ovaries of postnatal mice. In line with these data, the depletion experiments showed that MHC II$^-$ MAC 1 cells are the first bone marrow-derived cell type recovered in experimentally emptied ovarian niche. In addition, they can differentiate into MHC II intermediate and high macrophage types, MAC 2 and MAC 3, respectively. The concept of macrophage population interconversion in the ovaries is further supported by the trajectory analyses showing the close relationship between three macrophage subtypes in the ovaries under physiological conditions. Taken together, the phenotypic differences of interstitial macrophages, distinct molecular mechanisms of monocyte infiltration, and macrophage interconversion suggest that the concept of coexistence of two interstitial macrophage populations with specific subtissular niches

**Figure 5.** Bone marrow-derived macrophages have the capacity to produce all macrophage subtypes in an empty ovarian niche. (A) Flow cytometric analyses of macrophage populations in the ovaries of 5-week-old *Ccr2*$^{-/-}$ and *Nur77*$^{-/-}$ mice. Shown are quantifications of MAC 1 (MHC II$^{neg/low}$; orange), MAC 2 (MHC II$^{int}$; grey), and MAC 3 (MHC II$^{high}$; black) macrophage populations (n = 6-11 mice) All data are from two independent experiments. Bars represent the mean ± SEM of each group. (B) Experimental outline for depleting macrophages with anti-CSF-1 (αCSF1) and clodronate/control liposome treatment. i.p., intraperitoneal, i.v., intravenous, IgG, isotype-matched control antibody. (C) Numbers of MAC 1 (MHC II$^{neg/low}$), MAC 2 (MHC II$^{int}$), and MAC 3 (MHC II$^{high}$) in the ovaries of anti-CSF1+clodronate (αCSF1+Clod) treated and control antibody treated (Co) mice 48 h after the last treatment (Acute; n = 3-6 mice), after a 10-day recovery (n = 5-6 mice) and after a 3 week recovery (n = 2-3 mice) measured by flow cytometry. All data are from two independent experiments. Bars represent the mean ± SEM of each group (*$p < 0.05$, **$p < 0.01$, Mann–Whitney test). (D) Single-cell force-directed layout of the ovarian CD64$^+$F4/80$^+$ myeloid cells in 5-week-old WT mice. Based on the expression analyses of 10 myeloid cell selective markers (shown in E), grey boxes and coloring were manually added to visualize the different clusters. In this representative figure, all the samples from 5-week-old WT mice were overlaid. (E) Unsupervised hierarchial X-shift clustering (nearest neighbor) of CD64$^+$F4/80$^+$ myeloid cells in the ovaries of 5-week-old WT mice with superimposed expression analyses of the indicated leukocyte differentiation markers. Color code represents the expression levels of the indicated markers (blue means low and red high expression). All mass cytometry data are from three independent samples pooled from three individuals.

and lineages needs to be refined for certain tissues like the ovaries.

In conclusion, we have shown here that multiple tissue-resident monocyte and macrophage subsets coexist in the ovaries. Both embryonic and bone marrow-derived macrophages appear to acquire similar phenotypes in the ovaries, suggesting the dominant role of the tissue niche over the ontogenic origin in shaping the macrophage identity. The three oMφ subsets do not show apparent differences in intraorgan localization or in scavenging function. However, the clear difference in MHC II expression suggest that oMφ MAC 2 and, in particular, MAC 3 will have superior antigen presenting capacity when compared to MAC 1. Elucidation of the macrophage origin and differentiation in the mouse ovaries will pave the way for dissecting the contribution of local macrophage subsets to normal and pathological ovarian function in mice and humans.

## Materials and methods

### Animals

We have previously described the Plvap$^{tm1Salm}$ mice (referred as *Plvap*$^{-/-}$) used in this study [44, 56]. *Ccr2*$^{-/-}$ (stock 004999), *Nur77*$^{-/-}$ (stock 006187), R26R-EYFP (stock 006148), Cx3cr1-CreERT2 (stock 020940), and Csf1r-Mer-iCre-Mer (stock 019098) mice were obtained from The Jackson Laboratory. C57BL/6J and C57BL/6N mice were purchased from Janvier Labs.

Mice were housed under controlled environmental conditions (12 h light/12 h darkness) at the Central Animal Laboratory of the University of Turku. All animal experiments were approved by the National Animal Experiment Board in Finland, which fully met the requirements defined in the US National Institutes of Health guidelines on animal experimentation. They were carried out in adherence with the rules and regulations of the Finnish Act on Animal Experimentation (497/2013) and in accordance to the 3R-principle under Animal license number 6211/04.10.07/2017. Age-matched WT mice were used as controls in each experiment. Female mice were used in all analyses. Embryonic development was estimated considering the day of vaginal plug as embryonic day 0.5 (E0.5).

### Isolation of embryonic and adult cells

For isolating cells from embryonic tissues, pregnant females were sacrificed by carbon dioxide inhalation and cervical dislocation. Embryos from embryonic day (E) 14.5 to E17.5 were dissected out from uterus and placed in cold PBS (Invitrogen). Ovaries and brain were carefully dissected from the embryos. To obtain single cell suspensions, the ovaries were incubated in αMEM containing 1% FBS (Thermo Fisher Scientific), 1 mg/mL Collagenase I (Roche), 50 μg/mL deoxyribonuclease I (DNase I; Sigma-Aldrich) at +37°C in 5% CO$_2$ for 45 min and then filtered through silk (pore size 77 μm). The brain cells were resuspended in isotonic Percoll (GE Healthcare) and the microglia were isolated as previously described [44, 57].

The cells from the adult tissues were isolated in the same way as the embryonic cells, except with the following modifications that ovaries were mechanically dissociated by poking with two 25G needles and the enzymatic digestion was extended to 1 h.

### Mass cytometry staining, and data acquisition and processing

The cells were isolated from the ovaries as described above. In all stainings, ovaries from three mice (two ovaries/mouse) were pooled together. The cells were plated and stained in a U-bottom 96-well plate. To exclude dead cells, samples were stained with 250 μL of 2.5 μM Cell-ID Cisplatin (Fluidigm) at room temperature for 5 min [58]. After washings and Fc-blocking with anti-CD16/32, the cells were stained with heavy-metal isotope-labelled mAb cocktail (B220-159Tb, CD115-165Ho, CD117-173Yb, CD11b-148Nd, CD11c-142Nd, CD206-169Tm, CD274-153Eu, CD4-172Yb, CD45-175Lu, CD64-151Eu, CD80-171Yb, CD8a-168Er, CX3CR1-164Dy, F4/80-146Nd, Ly6C-162Dy, Ly6G-141Pr, MerTK-176Lu, MHC II-174Yb, Siglec1-170Er, and TER-119-154Sm) in 25 μL volume for 30 min at room temperature. The cells were then washed before a 1 h incubation at room temperature with intercalation solution (1:1000 Cell ID Intercalator-103Rh in MaxPar® Fix and Perm Buffer; Fluidigm). Finally, the stained cells were fixed with 250 μL of 4% paraformaldehyde solution (PFA; Santa Cruz Biotechnology) in PBS overnight and pelleted. Immediately prior to data acquisition using a CyTOF mass cytometer (Helios, Fluidigm), the cells were resuspended to MaxPar Water (Fluidigm).

Debarcoded and bead normalized mass cytometry data were exported as flow cytometry file (FCS) format into Cytobank [59]. Cells were gated for live (Cisplatin$^-$) singlets (Intercalator$^+$) to exclude debris and doublets. Gating, viSNE plots (dimensionality reduction algorithm t-SNE), and unsupervised clustering by Flow-SOM algorithm were performed with Cytobank platform (Cytobank, https://www.cytobank.org). For CD45$^+$ analyses, 10883-35922 events per sample were selected in total event sampling. The distinct CD45$^+$ cell populations were then manually assigned to different leukocyte subpopulations based on the expression of the known cell-type selective leukocyte differentiation markers. For CD45$^+$CD11b$^+$ viSNE analyses, 6092-14837 events per sample were selected in total event sampling. For CD64$^+$F4/80$^+$ viSNE analyses, 710-1839 events per sample were selected in total event sampling. To validate our findings, we performed unsupervised clustering of CD64$^+$F4/80$^+$ cells by self-organizing map (SOM) method using FlowSOM algorithm (version 1.4.0; 64 expected clusters). The number of metaclusters was determined by FlowSOM algorithm for a maximum of 14 clusters. After manually combining the unidentified clusters into one cluster, altogether nine clusters for CD64$^+$F4/80$^+$ cells were identified.

The mass cytometry data were also computationally clustered with X-shift algorithm [49] in VorteX platform (https://github.com/nolanlab/vortex/releases/tag/29-Jun-2017). All data events were merged into one dataset (different datasets by the age) and 3300–4300 total events were used in the analysis. The unsupervised hierarchical clustering X-shift algorithm was performed with 12 parameters using the default settings with nearest density estimation ($K$) from 150 to 10, with 30 steps and the elbow point ($K$) was calculated ($K = 67$ for 5-week-old and $K = 38$ for 12-week-old mice). All six clusters for 5-week-old and seven clusters for 12-week-old mice were selected and a force-directed layout was created (ForceAtlas2 algorithm; all cell events from clusters smaller than 1000 events, or 1000 randomly selected events from the clusters bigger than 1000 events). Two-dimensional figures were produced from the original three-dimensional data and the distinct CD64$^+$F4/80$^+$ cell clusters were then manually allocated to different leukocyte subpopulations based on the expression of the cell-type selective leukocyte differentiation markers. The layout and the visualization were produced with Gephi 0.9.1 (https://gephi.org).

## Flow cytometry analysis and cell sorting

Before the stainings, the cell suspensions were incubated with purified anti-CD16/32 (clone 2.4G2; Bio X Cell) for 10 min on ice to block nonspecific binding to Fc-receptors. Subsequently, fixable live/dead cell staining was performed according to manufacturer's instructions (Fixable Viability Dye eFluor 780; eBioscience). Stainings were performed at +4°C for 20 min with the following antibodies: anti-CD45-PerCP-Cy5,5 (clone 3O-F11; BD), anti-F4/80-A488 (clone BM8; eBioscience), anti-F4/80-A647 (clone Cl:A3-1; BioRad), anti-CD11b-BV786 (clone M1/70; BD), anti-Ly6C-BV421 (clone AL-21; BD), anti-CD64-PE (clone X54-5/7.1; BioLegend), anti-CD206-BV650 (clone C068C2; BioLegend), anti-MHC II-BV711 (clone M5/114.15.2; BD), anti-CD11c-BV421 (clone HL3; BD), anti-CD115-PE-Cy7 (clone AFS98; BioLegend), anti-Ly6G-BV510 (clone 1A8; BioLegend), anti-SiglecF-PE-CF594 (clone E50-2440; BD), and anti-MerTK-PE (clone 2B10C42; BioLegend). All FACS analyses were run using LSRFortessa flow cytometer (BD Biosciences) and analyzed using FlowJo (Tree Star Inc.) software.

Embryonic CD11b$^{int}$F4/80$^{high}$ (yolk sac-derived) and CD11b$^{high}$F4/80$^{Int}$ (fetal liver-derived) ovarian macrophage subpopulations were sorted for quantitative real-time PCR analyses using FACS aria II (70 μm nozzle, Beckton-Dickinson) cell sorter.

All flow cytometry experiments were conducted in line with the recently published guidelines [60].

## Uptake of immunocomplexes

Immune complexes were prepared by incubating ovalbumin OVA-Atto488 (41235 Sigma, 2 mg/mL in PBS) at 5:1 molar ratio with rabbit polyclonal anti-OVA IgG for 1 h at 4°C [61]. A total of 150 μL of OVA-anti-OVA antibody immunocomplex (SIC; 100 μg) was administrated *i.v.* (via tail vein injection) to WT mice of 5 weeks of age. As a control, mice were injected with PBS. Two hours after the injection, the recipient mice were sacrificed and the ovaries were harvested and processed for flow cytometry. To quantify the binding of immunocomplexes, the mean fluorescence intensity of Atto488 expression in the three MAC populations (and in CD206$^+$ and CD206$^{low/neg}$ MAC1 cells) was measured.

## Immunofluorescence stainings and microscopy

Ovaries were dissected and then fixed with 2% PFA in PBS for 30 min on ice. Dehydration was performed in an increasing series of methanol (up to 100%) at −20°C in preparation for whole mount (WM) samples. NB and 2-week-old old mice ovaries were used as entire organs, whereas vibratome sections (300 μm in thickness; Leica VT 1200 S) were prepared from the 5-week-old mice ovaries. Vibratome sectioning was done by first rehydrating the 2% PFA-fixed 5-week-old ovaries with 50% MeOH in PBS for 30 min. Afterward, the rehydration was completed with 100% PBS. Rehydrated ovaries were embedded in 4% agarose gel solution and cooled in an ice bath until solid. WM ovaries were rehydrated in 50% MeOH for 5 min and blocked with 0.5 % FCS, 1% BSA, and 0.4% Triton in PBS (PBS-BSA-T with serum). Incubation with primary antibody F4/80 (10 μg/mL in PBS-BSA-T; α-m clone C1 A3-1; BioXCell) was carried out with shaking at 4°C overnight. Subsequently, a secondary antibody (Goat anti-rat-A546, 4 μg/mL in PBS-BSA-T; A11081; Invitrogen) was added for another night. After careful washings, the WM samples were then incubated with MHC II-A488 (2 μg/mL in PBS-BSA-T; rat anti-mouse M5/114.15.2; 562352; BD) or CD206-A488 (2 μg/mL in PBS-BSA-T; rat anti-mouse MR5D3; MCA2235A488T; BioRad) and CD144-A647 (2 μg/mL in PBS-BSA-T; rat anti-mouse MR5D3; BD) antibodies. All antibody dilutions and washings between all staining steps were made with PBS-BSA-T. Finally, the samples were dehydrated with MeOH. Clearing was performed with benzyl alcohol/benzyl benzoate (BABB).

Microscopic imaging was performed using a 3i spinning disk confocal microscope (Intelligent Imaging Innovations) microscope equipped with a LD c-451 apochromat 40×/1.1 water objective and SlideBook 6 software (Intelligent Imaging Innovations) at room temperature with Yokogawa CSU-W1 scanner. All final images were maximum intensity projections of acquired z-planes. Background subtractions, linear brightness, and contrast adjustments, and median filtering for reduction of noise were performed with ImageJ software (National Institute of Health).

## Fate mapping experiments

To study embryonic origin CX3CR1$^+$ macrophages, CX3CR1$^{CreERT2}$ male mice were crossed with R26R-EYFP female mice. Pregnant females were administered intraperitoneally with one single dose of tamoxifen (1.5 mg/dam; Sigma-Aldrich) combined with

progesterone (0.75 mg/dam; Sigma-Aldrich) at E13.5 to induce the reporter recombination in the offspring. The contribution of yolk sac-derived CSF1R$^+$ cells was studied by crossing Csf1r-Mer-iCre-Mer mice with R26R-EYFP. Pregnant females were treated with tamoxifen and progesterone at E8.5. The pups were sacrificed either at birth, or in the age of 2 or 5 weeks for flow cytometric detection of the converted cells.

## Quantitative PCR

Total RNA was isolated from sorted ovarian macrophages of E16.5 WT embryos using the RNeasy Plus Micro kit (QIAGEN). The RNA was reverse transcribed to cDNA with SuperScript VILO cDNA Synthesis Kit (Thermo Fisher Scientific) according to the manufacturer's instructions. Quantitative PCR was carried out using Taqman Gene Expression Assays (ThermoFisher Scientific) for *Cx3cr1* (Mm00438354_m1), *Adgre1* (Mm00802529_m1, also known as *Emr1* or F4/80), *Itgam* (Mm00434455_m1), *Gata2* (Mm00492301_m1), *Flt3* (Mm00439016_m1), *Ccr2* (Mm04207877_m), *Csf1r* (Mm01266652_m1), and *Actb* (Mm02619580_g1; control gene).

The reactions were run using QuantStudio$^{TM}$ 12K Flex Real-Time PCR System (LifeTechnologies/Thermo Fisher Scientific) at the Finnish Microarray and Sequencing Centre (FMSC), Turku Bioscience Centre. Relative expression levels were calculated using QuantStudio$^{TM}$ 12 K Flex software (LifeTechnologies/ThermoFisher Scientific). The results were presented as percentages of control gene mRNA levels from the same samples.

## Macrophage depletion

To ablate the yolk sac-derived macrophages from the offspring, pregnant C57BL/6N females at E6.5 were treated with a single *i.p.* injection of a neutralizing CSF1R (clone AFS98; Bio X Cell) or rat IgG2a control antibody (clone 2A3; Bio X Cell) (3 mg of each antibody in sterile PBS). Mice were sacrificed at E17.5 or at the postnatal age of 2 weeks for flow cytometric analyses.

To deplete tissue resident macrophages postnatally, 2-week-old C57BL/6N mice were treated with three *i.p.* doses of CSF1 neutralizing antibody (clone 5A1; Bio X Cell) or control IgG (clone HRPN; Bio X Cell; 0.5 mg on postnatal day 14, 0.25 mg on days 18 and 22), and three *i.v.* doses of clodronate liposomes or control liposomes (Liposoma; 50 uL/each on postnatal days 15, 19, and 23) as outlined in Fig. 5B. The mice were sacrificed 48 h (acute), 10 days or 3 weeks after completing the dosing regimen.

For histologic analysis, the ovaries were obtained from mice 10 days after completing the dosing. The tissues were fixed at room temperature for overnight with 4% PFA and were then dehydrated and embedded in paraffin. For microscopic analysis, sections were cut 5-μm-thick and stained with hematoxylin and eosin. The quantification of ovarian follicles was performed from consecutive histologic sections of 5 CSF1 antibody + clodronate liposome-treated and 4 IgG + control liposome-treated WT mice. The morphologic

classification of follicles was carried out according a previously described staging [62], and each histologic section was compared with previous and sequential sections to prevent counting the same follicles more than once.

## Statistics

Adult mice were allocated to experimental groups without specific randomization methods, because comparisons involved mice of distinct genotypes. The researchers were blinded to the genotype of the embryos during the experimental procedure. Statistical analyses were carried out using GraphPad Prism software version 8 (GraphPad software Inc). All data are presented as mean values ± SEM. Statistical significances between groups, which was set at $p < 0.05$, was determined using Mann–Whitney test, two-way ANOVA followed with Bonferroni's post-hoc test or Kruskal–Wallis test followed with Dunn's post-hoc test.

**Conflict of interest:** The authors declare no financial or commercial conflict of interest.

## References

1 **Petrovska, M., Dimitrov, D. G. and Michael, S. D.,** Quantitative changes in macrophage distribution in normal mouse ovary over the course of the estrous cycle examined with an image analysis system. *Am. J. Reprod. Immunol.* 1996. **36**: 175–183.

2 **Best, C. L., Pudney, J., Welch, W. R., Burger, N. and Hill, J. A.,** Localization and characterization of white blood cell populations within the human ovary throughout the menstrual cycle and menopause. *Hum. Reprod.* 1996. **11**: 790–797.

3 **Hume, D. A. and Gordon, S.,** The mononuclear phagocyte system of the mouse defined by immunohistochemical localisation of antigen F4/80. In van Furth, R. (Ed.), *Mononuclear phagocytes: Characteristics, physiology and function*, Springer Netherlands, Dordrecht, 1985, pp. 9–18.

4 **Takaya, R., Fukaya, T., Sasano, H., Suzuki, T., Tamura, M. and Yajima, A.,** Macrophages in normal cycling human ovaries: immunohistochemical localization and characterization. *Hum. Reprod.* 1997. **12**: 1502–1512.

5 **Duncan, W. C., Rodger, F. E. and Illingworth, P. J.,** The human corpus luteum: reduction in macrophages during simulated maternal recognition of pregnancy. *Hum. Reprod.* 1998. **13**: 2435–2442.

6 Li, X. Q., Itoh, M., Yano, A., Xie, Q., Miyamoto, K. and Takeuchi, Y., Distribution of F4/80-positive cells in developing ovaries in the mouse. *Arch. Histol. Cytol.* 1998. **61**: 353–360.

7 Fukumatsu, Y., Katabuchi, H., Naito, M., Takeya, M., Takahashi, K. and Okamura, H., Effect of macrophages on proliferation of granulosa cells in the ovary in rats. *J. Reprod. Fertil.* 1992. **96**: 241–249.

8 Petrovska, M., Sedlak, R., Nouza, K., Presl, J. and Kinsky, R., Development and distribution of the white blood cells within various structures of the human menstrual corpus luteum examined using an image analysis system. *Am. J. Reprod. Immunol.* 1992. **28**: 77–80.

9 Fukumatsu, Y., Katabuchi, H. and Okamura, H., Immunohistochemical localization of epidermal growth factor and its effect on granulosa cell proliferation in rat ovary. *Endocr. J.* 1995. **42**: 467–473.

10 Katabuchi, H., Fukumatsu, Y., Araki, M., Suenaga, Y., Ohtkae, H. and Okamura, H., Role of macrophages in ovarian follicular development. *Horm. Res. Paediatr.* 1996. **46**: 45–51.

11 Van der Hoek, K. H., Maddocks, S., Woodhouse, C. M., van Rooijen, N., Robertson, S. A. and Norman, R. J., Intrabursal injection of clodronate liposomes causes macrophage depletion and inhibits ovulation in the mouse ovary. *Biol. Reprod.* 2000. **62**: 1059–1066.

12 Brännström, M. and Enskog, A., Leukocyte networks and ovulation. *J. Reprod. Immunol.* 2002. **57**: 47–60.

13 Ingman, W. V. and Robertson, S. A., Defining the actions of transforming growth factor beta in reproduction. *BioEssays* 2002. **24**: 904–914.

14 Wu, R., Van der Hoek, K. H., Ryan, N. K., Norman, R. J. and Robker, R. L., Macrophage contributions to ovarian function. *Hum. Reprod. Update.* 2004. **10**: 119–133.

15 Carlock, C., Wu, J., Zhou, C., Ross, A., Adams, H. and Lou, Y., Ovarian phagocyte subsets and their distinct tissue distribution patterns. *Reproduction.* 2013. **146**: 491–500.

16 Yoshida, H., Hayashi, S. I., Kunisada, T., Ogawa, M., Nishikawa, S., Okamura, H., Sudo, T. et al., The murine mutation osteopetrosis is in the coding region of the macrophage colony stimulating factor gene. *Nature* 1990. **345**: 442–444.

17 Cohen, P. E., Zhu, L., Nishimura, K. and Pollard, J. W., Colony-stimulating factor 1 regulation of neuroendocrine pathways that control gonadal function in mice. *Endocrinology* 2002. **143**: 1413–1422.

18 Pollard, J., Hunt, J., Wiktor-Jedrzejczac, W. and Stanley, E., A pregnancy defect in the osteopetrotic (op/op) mouse demonstrates the requirements for CSF-1 in female fertility. *Dev. Biol.* 1991. **148**: 273–283.

19 Cailhier, J. F., Partolina, M., Vuthoori, S., Wu, S., Ko, K., Watson, S., Savill, J. et al., Conditional macrophage ablation demonstrates that resident macrophages initiate acute peritoneal inflammation. *J. Immunol.* 2005. **174**: 2336–2342.

20 Turner, E. C., Hughes, J., Wilson, H., Clay, M., Mylonas, K. J., Kipari, T., Duncan, W. C. et al., Conditional ablation of macrophages disrupts ovarian vasculature. *Reproduction.* 2011. **141**: 821–831.

21 Králíčková, M. and Vetvicka, V., Immunological aspects of endometriosis: a review. *Ann Transl Med.* 2015. **3**: 153.

22 Wu, J., Xie, H., Yao, S. and Liang, Y., Macrophage and nerve interaction in endometriosis. *J. Neuroinflam.* 2017. **14**: 1–11.

23 Volkman, A. and Gowans, J. L., The origin of macrophages from bone marrow in the rat. *Br. J. Exp. Pathol.* 1965. **46**: 62–70.

24 van Furth, R. and Cohn, Z. A., Origin and kinetics of mononuclear phagocytes. *J. Exp. Meidicine.* 1968. **128**: 415–435.

25 Hoeffel, G., Wang, Y., Greter, M., See, P., Teo, P., Malleret, B., Leboeuf, M. et al., Adult Langerhans cells derive predominantly from embryonic fetal liver monocytes with a minor contribution of yolk sac-derived macrophages. *J. Exp. Med.* 2012. **209**: 1167–1181.

26 Guilliams, M., De Kleer, I., Henri, S., Post, S., Vanhoutte, L., De Prijck, S., Deswarte, K. et al., Alveolar macrophages develop from fetal monocytes that differentiate into long-lived cells in the first week of life via GM-CSF. *J. Exp. Med.* 2013. **210**: 1977–1992.

27 Hashimoto, D., Chow, A., Noizat, C., Teo, P., Beasley, M. B., Leboeuf, M., Becker, C. D. et al., Tissue-resident macrophages self-maintain locally throughout adult life with minimal contribution from circulating monocytes. *Immunity.* 2013. **38**: 792–804.

28 Kim, K. W., Williams, J. W., Wang, Y. T., Ivanov, S., Gilfillan, S., Colonna, M., Virgin, H. W. et al., MHC II⁺ resident peritoneal and pleural macrophages rely on IRF4 for development from circulating monocytes. *J. Exp. Med.* 2016. **213**: 1951–1959.

29 Shaw, T. N., Houston, S. A., Wemyss, K., Bridgeman, H. M., Barbera, T. A., Zangerle-Murray, T., Strangward, P. et al., Tissue-resident macrophages in the intestine are long lived and defined by Tim-4 and CD4 expression. *J. Exp. Med.* 2018. **215**: 1507–1518.

30 Dick, S. A., Macklin, J. A., Nejat, S., Momen, A., Clemente-Casares, X., Althagafi, M. G., Chen, J. et al., Self-renewing resident cardiac macrophages limit adverse remodeling following myocardial infarction. *Nat. Immunol.* 2019. **20**: 29–39.

31 Amir, E. A. D., Davis, K. L., Tadmor, M. D., Simonds, E. F., Levine, J. H., Bendall, S. C., Shenfeld, D. K. et al., ViSNE enables visualization of high dimensional single-cell data and reveals phenotypic heterogeneity of leukemia. *Nat. Biotechnol.* 2013. **31**: 545–552.

32 Van Gassen, S., Callebaut, B., Van Helden, M. J., Lambrecht, B. N., Demeester, P., Dhaene, T. and Saeys, Y., FlowSOM: using self-organizing maps for visualization and interpretation of cytometry data. *Cytom. Part A.* 2015. **87**: 636–645.

33 Faraco, G., Sugiyama, Y., Lane, D., Garcia-Bonilla, L., Chang, H., Santisteban, M. M., Racchumi, G. et al., Perivascular macrophages mediate the neurovascular and cognitive dysfunction associated with hypertension. *J. Clin. Invest.* 2016. **126**: 4674–4689.

34 Schyns, J., Bai, Q., Ruscitti, C., Radermecker, C., De, S. S., Chakarov, S., Farnir, F. et al., Non-classical tissue monocytes and two functionally distinct populations of interstitial macrophages populate the mouse lung. *Nat. Commun.* 2019. **10**: 1–16.

35 Munro, D. A., Wineberg, Y., Tarnick, J., Vink, C. S., Li, Z., Pridans, C., Dzierzak, E. et al., Macrophages restrict the nephrogenic field and promote endothelial connections during kidney development. *Elife.* 2019. **8**: 1–27.

36 Schulz, C., Perdiguero, E. G., Chorro, L., Szabo-Rogers, H., Cagnard, N., Kierdorf, K., Prinz, M. et al., A lineage of myeloid cells independent of Myb and hematopoietic stem cells. *Science.* 2012. **336**: 86–90.

37 Yona, S., Kim, K. W., Wolf, Y., Mildner, A., Varol, D., Breker, M., Strauss-Ayali, D. et al., Fate mapping reveals origins and dynamics of monocytes and tissue macrophages under homeostasis. *Immunity.* 2013. **38**: 79–91.

38 Varol, C., Mildner, A. and Jung, S., Macrophages: development and tissue specialization. *Annu. Rev. Immunol.* 2015. **33**: 643–675.

39 Ginhoux, F. and Guilliams, M., Tissue-resident macrophage ontogeny and homeostasis. *Immunity* 2016. **44**: 439–449.

40 Perdiguero, E. G. and Geissmann, F., The development and maintenance of resident macrophages. *Nat. Immunol.* 2016. **17**: 2–8.

41 Molawi, K., Wolf, Y., Kandalla, P. K., Favret, J., Hagemeyer, N., Frenzel, K., Pinto, A. R. et al., Progressive replacement of embryo-derived cardiac macrophages with age. *J. Exp. Med.* 2014. **211**: 2151–2158.

42 Hoeffel, G., Chen, J., Lavin, Y., Low, D., Almeida, F. F., See, P. and Beaudin, A. E. et al., C-Myb⁺ erythro-myeloid progenitor-derived fetal monocytes

give rise to adult tissue-resident macrophages. *Immunity*. 2015. **42**: 665–678.

43  **Squarzoni, P., Oller, G., Hoeffel, G., Pont-Lezica, L., Rostaing, P., Low, D. and Bessis, A. et al.**, Microglia modulate wiring of the embryonic forebrain. *Cell Rep.* 2014. **8**: 1271–1279.

44  **Rantakari, P., Jäppinen, N., Lokka, E., Mokkala, E., Gerke, H., Peuhu, E. and Ivaska, J. et al.**, Fetal liver endothelium regulates the seeding of tissue-resident macrophages. *Nature*. 2016. **538**: 392–396.

45  **Boring, L., Gosling, J., Chensue, S. W., Kunkel, S. L., Farese, R. V., Broxmeyer, H. E. and Charo, I. F.**, Impaired monocyte migration and reduced type 1 (Th1) cytokine responses in C-C chemokine receptor 2 knockout mice. *J. Clin. Invest.* 1997. **100**: 2552–2561.

46  **Hanna, R. N., Carlin, L. M., Hubbeling, H. G., Nackiewicz, D., Green, A. M., Punt, J. A., Geissmann, F. et al.**, The transcription factor NR4A1 (Nur77) controls bone marrow differentiation and the survival of Ly6C-monocytes. *Nat. Immunol.* 2011. **12**: 778–785.

47  **Zhu, Y., Herndon, J. M., Sojka, D. K., Fields, R. C., Randolph, G. J., Denardo, D. G., Zhu, Y. et al.**, Tissue-resident macrophages in pancreatic ductal adenocarcinoma originate from embryonic hematopoiesis and promote tumor progression. *Immunity* 2017. **47**: 323–338.

48  **Jäppinen, N., Félix, I., Lokka, E., Pynttäri, A., Lahtela, T., Gerke, H., Elima, K. et al.**, Fetal-derived macrophages dominate in adult mammary glands. *Nat. Commun.* 2019. **10**: 1–12.

49  **Samusik, N., Good, Z., Spitzer, M. H., Davis, K. L. and Nolan, G. P.**, Automated mapping of phenotype space with single-cell data. *Nat. Methods*. 2016. **13**: 493–499.

50  **Bertrand, J. Y., Desanti, G. E., Lo-Man, R., Leclerc, C., Cumano, A. and Golub, R.**, Fetal spleen stroma drives macrophage commitment. *Development* 2006. **133**: 3619–3628.

51  **Iseki, A., Morita, Y., Nakauchi, H. and Ema, H.**, Hematopoietic stem cells in the mouse spleen. *Blood*. 2008. **112**: 2421.

52  **Tanaka, Y., Inoue-Yokoo, T., Kulkeaw, K., Yanagi-Mizuochi, C., Shirasawa, S., Nakanishi, Y. and Sugiyama, D.**, Embryonic hematopoietic progenitor cells reside in muscle before bone marrow hematopoiesis. *PLoS One*. 2015. **10**: 1–19.

53  **Medvinsky, A. and Dzierzak, E.**, Definitive hematopoiesis is autonomously initiated by the AGM region. *Cell*. 1996. **86**: 897–906.

54  **Chakarov, S., Lim, H. Y., Tan, L., Lim, S. Y., See, P., Lum, J., Zhang, X. M. et al.**, Two distinct interstitial macrophage populations coexist across tissues in specific subtissular niches. *Science*. 2019. **363**: eaau0964.

55  **Barreiro, O., Cibrian, D., Clemente, C., Alvarez, D., Moreno, V., Valiente, Í., Bernad, A. et al.**, Pivotal role for skin transendothelial radio-resistant anti-inflammatory macrophages in tissue repair. *Elife*. 2016. **5**: 1–33.

56  **Rantakari, P., Auvinen, K., Jäppinen, N., Kapraali, M., Valtonen, J., Karikoski, M., Gerke, H. et al.**, The endothelial protein PLVAP in lymphatics controls the entry of lymphocytes and antigens into lymph nodes. *Nat. Immunol.* 2015. **16**: 386–396.

57  **Ginhoux, F., Greter, M., Leboeuf, M., Nandi, S., See, P., Gokhan, S., Mehler, M. F. et al.**, Fate mapping analysis reveals that adult microglia derive from primitive macrophages. *Science*. 2010. **701**: 841–845.

58  **Fienberg, H. G., Simonds, E. F., Fantl, W. J., Nolan, G. P. and Bodenmiller, B.**, A platinum-based covalent viability reagent for single-cell mass cytometry. *Cytom. Part A*. 2012. **81 A**: 467–475.

59  **Nikesh, K., Krutzik, P. O. and Irish, J. M.**, Web-based analysis and publication of flow cytometry experiments. *Curr. Protoc. Cytom.* 2010. **53**: 1–40.

60  **Cossarizza, A., Chang, H. D., Radbruch, A., Acs, A., Adam, D., Adam-Klages, S., Agace, W. W. et al.**, Guidelines for the use of flow cytometry and cell sorting in immunological studies (second edition). *Eur. J. Immunol.* 2019. **49**: 1457–1973.

61  **Stamatiades, E. G., Tremblay, M. E., Bohm, M., Crozet, L., Bisht, K., Kao, D., Coelho, C. et al.**, Immune monitoring of trans-endothelial transport by kidney-resident macrophages. *Cell*. 2016. **166**: 991–1003.

62  **Myers, M., Britt, K. L., Wreford, N. G. M., Ebling, F. J. P. and Kerr, J. B.**, Methods for quantifying follicular numbers within the mouse ovary. *Reproduction*. 2004. **127**: 569–580.

*Abbreviations:* **NB**: newborn · **PFA**: paraformaldehyde solution · **WM**: whole mount

*Full correspondence:* Dr. Pia Rantakari, Turku Bioscience Centre, University of Turku, Tykistökatu 6B, 20520 Turku Finland
e-mail: pia.rantakari@utu.fi
and
Prof. Marko Salmi, MediCity Research Laboratory, University of Turku, Tykistökatu 6A, 20520 Turku Finland
e-mail: marko.salmi@utu.fi